sciendo

POLISH MARITIME RESEARCH 4 (124) 2024 Vol. 31; pp. 131-141
10.2478/pomr-2024-0057

Experimental Study and Numerical Simulation of Radiated Noise from Unmanned Underwater Vehicle

Chunyu Zhang [1]
Qiang Xu [1*]
He Yang [1]
Zilong Peng [1]
Jiangqiao Li [2]
Jialiang Zhou [3]
[1] Jiangsu University of Science and Technology, Zhenjiang, China
[2] Systems Engineering Research Institute, Beijing, China
[2] China Ship Development and Design Center, Wuhan, China

* Corresponding author: *1084141135@qq.com (Qiang Xu)*

ABSTRACT

This paper focuses on the research of the radiation noise of underwater unmanned vehicle (UUV), which is one of the most important indicators for evaluating the performance of underwater unmanned equipment. Integrating experimental study and numerical calculations, this paper investigates the underwater radiated noise characteristics and hydrodynamic properties of the propeller of UUV. Firstly, an open-water radiated noise experiment is conducted. To ensure the accuracy of acoustic test, the UUV are held stationary during the experiment. Then, the hydrodynamic performance of a propeller in a steady flow field is calculated using Computational Fluid Dynamics (CFD). Finally, the noise in the unsteady flow field is calculated using the Ffowcs Williams-Hawkings (FW-H) equation. The results show that the propeller, as the main noise source when the UUV is working, exhibits distinct characteristic line spectra in the frequency response curve. By comparing the numerical and experimental results, it was found that the overall trend of the sound pressure level is similar. But the line spectrum characteristics of the numerical results between 100 and 400 Hz are more obvious, mainly because the simulation model is more idealized compared to the experimental tests. The study further examines the hydrodynamic characteristics, propeller noise, and directional characteristics of UUV under different operating conditions.

Keywords: UUV; noise of propeller; UUV acoustic radiation; acoustic radiation experiment

INTRODUCTION

In current marine engineering applications, unmanned underwater vehicle (UUV) are widely utilized as an essential tool in various fields such as marine ecological conservation, environmental monitoring, and sustainable ocean resource development [1]. Meanwhile, UUVs have played a crucial role in military security due to their advantages such as small size, wide distribution, and low noise. They contribute significantly to intelligence gathering, early warning surveillance, military defense, and other related areas [2]. However, with the increasing use of UUV, the issue of underwater radiated noise has drawn significant attention.

Underwater radiated noise may potentially impact the ecological balance and behavior of marine organisms, as well as interfere with the accuracy of environmental monitoring equipment [3,4]. Therefore, analyzing the characteristics of UUV underwater radiated noise has become crucial, which is essential to solving the problems in the overall noise reduction of UUV.

The theoretical prediction methods for propeller noise represent a complex and important research area, which has

made remarkable progress under extensive research by some scholars. These theoretical methods have evolved from the initial momentum theory to the current Computational Fluid Dynamics (CFD) calculations, combined with Computational Aeroacoustics (CAA) for acoustic analysis. The research process primarily consists of two steps. First, obtaining the hydrodynamic performance of the propeller, including the pressure distribution on the blade surfaces and the flow field around the propeller, through experiments or theoretical calculations. Then, using these data as the sound source, combined with CFD and CAA methods, to predict and analyze the radiated noise. This coupled approach can more accurately calculate the generation mechanism of propeller noise and provide important references for optimizing propeller design. Continuous improvements and refinements of these theoretical prediction methods enhance the understanding and control of underwater propeller noise, thereby improving the stealth and operational effectiveness of UUV.

At present research in the area of theoretical prediction methods for propeller noise has been extensively conducted by scholars both domestically and internationally. As the primary noise source of underwater vehicles, the radiated noise from propellers has been a focal point in the field [5]. The theoretical approaches have progressed from the initial momentum theory to the current CFD methodologies. The research typically unfolds in two phases. Initially, the hydrodynamic performance of the propeller is determined through experiments or theoretical calculations, followed by the computation of radiated noise using the obtained pressure distribution on the propeller blades and the surrounding flow field as the noise source. Si et al. [6] employed a combination of numerical calculations and experimental studies to investigate the noise generation mechanisms and the acoustic field distribution characteristics of ducted propellers, providing theoretical references for the suppression of dynamic noise in underwater robots and their acoustic optimization design. Wang [7] conducted computational analyses of unmanned vehicle propeller noise, hydrodynamic noise, and mechanical noise using empirical formulae, CFD, and Finite Element Methods. Liu [8] analyzed the dynamic characteristics of propulsion motors based on Finite Element Methods, offering references for modeling the excitation sources in UUV. Sebastian et al. [9] carried out numerical simulation and cavitation water tunnel tests on the CP469 paddle model. They used a stern companion. The velocity distribution of the flow field was calculated as the method of the initial condition of the propeller flow, and the cavitation test was carried out under the same condition research. This study confirms the reliability of the numerical results. Anirban et al. [10] proposed a practical scaling method for systematic CFD calculations of adjustable pitch ducted propellers with two different designs. Deng et al. [11] simulated the hydrodynamic and noise performance of common pump-jet ducted propeller models and serrated tube pump-jet ducted propeller models in underwater vehicles, studied the effects of serrated ducts on the hydrodynamic and noise performance of pump-jet s, and predicted the noise of the models using CFD software. Chen et al. [12] analyzed the frequency domain characteristics and directivity of sound pressure levels at different acoustic field monitoring points for ducted propellers at four speeds using the FW-H equation. Kimmerl et al. [13] used Implicit Large Eddy Simulation (LES) to evaluate tip and hub vortex cavitation. Comparing the cavitation structure of a free-running propeller simulated by implicit LES with experimental measurements, we found that implicit LES effectively resolves the turbulent details and bubble structures of free-running propellers. Chamanar et al. [14] simulated the hydrodynamic characteristics of a ducted propeller using different turbulence models and compared and discussed the results with experimental data. Zhang et al. [15] developed a new method that integrates Open Prop with CFD to design the propeller for the Explorer 100 AUV, and based on CFD methods, they analyzed its flow field and hydrodynamic characteristics.

It is widely acknowledged that cavitation of propellers in seawater constitutes a primary source of noise for ships. The high-speed rotation of propellers leads to pressure drops in the water, resulting in the formation and collapse of cavitation bubbles, which directly emit acoustic energy into the water. Lee et al. [16] introduced a model test process and scaling method to predict the full-scale equivalent reference noise level of hydrodynamic noise sources. The effectiveness of this method was validated through experiments and simulations. Viitanen et al. [17] studied the performance and cavitation characteristics of marine propellers under oblique flow conditions in unsteady flow fields using CFD methods. Ku et al. [18] utilized a Computational Hydro-acoustics (CHA) approach to predict the hydrodynamic noise caused by Tip Vortex Cavitation (TVC) of submarine propeller blades underwater, where the influence of the nominal wake field generated by the submarine hull on TVC was also investigated.

In the field of UUV acoustic testing, a handful of scholars have conducted research. Railey [19] carried out underwater noise tests for multiple models of UUVs, focusing on the radiated noise from propulsion motors at various propeller speeds and velocities, aiming to infer information such as the UUV's speed from the noise measurements. Gebbie [20] deployed a hydrophone array vertically in waters near Honolulu Harbor to conduct the first propulsor noise tests under the operational conditions of UUVs and introduced the UUV source level based on the OASES method. Yu [21] combined CFD and FEM for simulating and predicting the hydrodynamic noise of UUVs and conducted underwater acoustic radiation experiments. The study indicated that the simulation predictions aligned well with experimental results before propeller cavitation occurred, but the accuracy significantly decreased once cavitation effects emerged. Zakeri et al. [22] presented the dynamic modeling of a mini-unmanned underwater vehicle and calculated its hydrodynamic characteristics by CFD software. Su et al. [23] studied the unsteady hydrodynamic characteristics of pump-jet under the wake of the SUBOFF model, and the vibration acoustic characteristics of pump-jet shafting SUBOFF model under unsteady excitation. By applying distributed or equivalent pulse force to different regions of the pump-jet, the influence of the method of applying excitation force on the vibration and sound response is studied. Wang et al. [24] evaluated the self-noise characteristics of Petrel acoustic AUVs through simulation and testing. Additionally, acoustic radiation experiments were conducted in an anechoic

chamber and the South China Sea. Sun et al. [25] developed a sound wave glider for environmental noise measurement and target detection in the ocean, by deploying acoustic vector sensors (AVS). Field trials have confirmed that the sound wave glider is capable of undertaking a wide range of underwater acoustic measurement and detection tasks. Krystian [26] analyzed the frequency characteristics of noise generated by moving vessels, exploring possibilities for acoustic classification of ships and diagnostic mechanisms of sound sources.

Despite the extensive research conducted by scholars on the acoustic radiation characteristics of propellers and yielding numerous significant findings, present studies predominantly focus on large propeller structures. Research on the acoustic radiation characteristics of miniature propellers used in UUV remains relatively scarce. This paper conducts numerical simulations of the acoustic radiation from miniature-scale propellers and underwater acoustic radiation experiments on UUV. By employing a combined approach of simulation and experimentation, the study focuses on investigating the acoustic characteristics of UUVs and miniature-scale propellers, as well as the hydrodynamic properties of miniature-scale propellers. The structure of the paper is as follows: in section 2, the selection of turbulence model and the introduction of acoustic equations in numerical simulation were introduced in detail. In section 3, experiment subjects and experiment procedures were introduced in detail. In section 4, modeling of research objects and setting of boundary conditions in simulation were introduced in detail. In section 5, the experimental results and simulation results were analyzed and compared respectively. The conclusion is made finally.

NUMERICAL METHODOLOGY OF THE HYDRODYNAMIC NOISE

GOVERNING EQUATION

Throughout the simulation process, the principles of mass conservation, energy conservation, and momentum conservation should be followed. The fluid medium in the simulation is exclusively water, characterized by its incompressibility and the absence of thermal exchange. The governing equations for the unsteady Reynolds-averaged Navier-Stokes (RANS) can be expressed as follows mass and momentum conservation equations:

$$\frac{\partial(\mu_i)}{\partial x_i} = 0 \tag{1}$$

$$\rho \frac{\partial(u_i u_j)}{\partial x_j} = -\frac{\partial p}{\partial x_j} + \rho \frac{\partial}{\partial x_j}\left[\mu\left(\frac{\partial u_i}{\partial x_j} + \frac{\partial u_j}{\partial u_i}\right) - \overline{\mu_i' \mu_j'}\right] \tag{2}$$

In the equation, $u_i u_j$ represent the mean values of the velocity components (i,j = 1,2,3). p denotes the mean pressure, ρ stands for the fluid density, μ is the viscosity coefficient of the fluid. $-\rho\mu_i'\mu_j'$ refers to the Reynolds stress term.

TURBULENCE MODEL

Kolmogorov posited that in addition to considering the turbulent kinetic energy, another variable ω should be taken into account. This variable represents the energy dissipation per unit volume per unit time. The inverse of ω denotes the timescale of turbulence, while k-ω is akin to the turbulence dissipation rate ε. In 1942, Kolmogorov developed partial differential equations for k and ω, marking the inception of the earliest two-equation turbulence model. The shear stress transport (SST) k-ω model combines the advantages of both the k-ε and k-ω models, rendering it suitable for various flow conditions. It employs the k-ω model near the wall to capture the turbulent behavior of the boundary layer, while the k-ε model is used to simulate the free-stream regions further from the wall. This model is appropriate for simulating turbulence near the wall and in free-stream areas, achieving good accuracy at lower computational costs. However, it may exhibit prediction inaccuracies or fail in certain specific scenarios, necessitating validation and adjustments with experimental data.

The fundamental equations of the SST k-ω model include the k equation and the ω equation as follows:

$$\frac{\partial}{\partial x_i}(\rho k u_i) + \frac{\partial(\rho k)}{\partial t} = \frac{\partial}{\partial x_j}\left(\Gamma_k \frac{\partial k}{\partial x_j}\right) + G_k - Y_k + S_k \tag{3}$$

$$\frac{\partial}{\partial x_i}(\rho \bar{\omega} u_i) + \frac{\partial(\rho \bar{\omega})}{\partial t} = \frac{\partial}{\partial x_j}\left(\Gamma_{\bar{\omega}} \frac{\partial \bar{\omega}}{\partial x_j}\right) + G_{\bar{\omega}} - Y_{\bar{\omega}} + S_{\bar{\omega}} \tag{4}$$

In the equations, k represents the turbulent kinetic energy, and ω denotes the dissipation rate. Γ_k and $\Gamma_{\bar{\omega}}$ are the effective diffusion coefficients for k and ω respectively, Y_k and $Y_{\bar{\omega}}$ are the dissipation of k and ω under the effect of turbulence. G_k is the production term of k, $D_{\bar{\omega}}$ is the cross-diffusion term, S_k and $S_{\bar{\omega}}$ are custom sources.

ACOUSTIC SIMULATION METHODOLOGY

The FW-H equation is derived from the continuity and momentum equations of fluid dynamics, based on the expansion of Lighthill's theory. This makes the FW-H equation broader in foundation and more widely applicable. By jointly solving the derived fluid continuity equation and the fluid momentum equation after taking the divergence, and eliminating the convection terms, it transforms into a sourced wave equation, known as the FWH equation, as follows:

$$\left[\frac{1}{c_0^2}\frac{\partial^2}{\partial t^2} - \frac{\partial^2}{\partial x_i^2}\right][Hc_0^2(p-p_0)] = \frac{\partial}{\partial t}[Q|\nabla f|\delta(f)] - \frac{\partial}{\partial x_i}[L_i|\nabla f|\delta(f)] + \frac{\partial^2(HT_{ij})}{\partial x_i x_j} \tag{5}$$

In the equation:

$$L_i = \left[(p-p_0)\delta_{ij} - \tau_{ij} + \rho u_i(u_j - v_j)\right] n_j \tag{6}$$

$$T_{ij} = \rho u_i u_j + \left[(p-p_0) - c_0^2(p-p_0)\right]\delta_{ij} - \tau_{ij} \tag{7}$$

$$Q = \frac{\rho u_i}{\rho_0} + \left[1 - \frac{\rho}{\rho_0}\right] v_i \tag{8}$$

$$H\left[f\left[\vec{x},t\right]\right]=\begin{cases}1, f\left[\vec{x},t\right]>\\ 0, f\left[\vec{x},t\right]<\end{cases} \quad (9)$$

In the equations, f represents the equation of a solid surface: within the solid $f < 0$, on the surface $f = 0$, and outside $f > 0$. u_i is the fluid velocity, v_i is the solid surface velocity. ρ_0 , p_0, and c_0 represent the far-field fluid density, pressure, and speed of sound, respectively. With $p = p_0 + p'$ being the local fluid pressure, where p' is the pressure fluctuation, equating to the acoustic pressure at a distance. The right side of equation (5) first term is a monopole source on the body surface, known as monopole noise or thickness noise. And the second term is a dipole source, referred to as dipole noise or loading noise. The third term is a quadrupole source, known as quadrupole noise.

RESEARCH OBJECT

TESTING EQUIPMENT

The experimental study focused on a UUV model, constructed from 6061 aluminum alloy with a shell thickness of 8.5 mm, as illustrated in Fig. 1. The fore and aft sections were made of ABS material, while the wings were crafted from carbon fiber. The UUV was assembled from four compartments from the bow to the stern, with lengths of 385 mm, 495 mm, 620 mm, and 495 mm, respectively. The diameter of the cabin is 221 mm. The propeller used in the UUV is Model 260, manufactured by Tecnadyne.

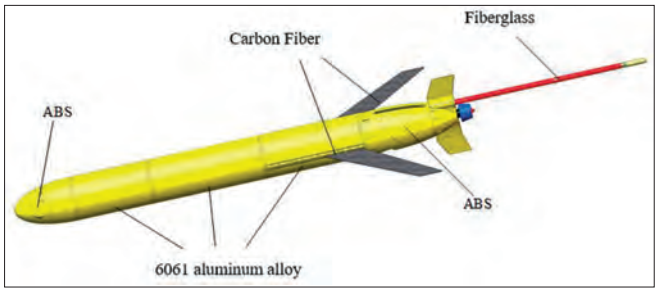

Fig. 1. Schematic diagram of UUV model

The primary experimental testing equipment includes: Reson TC 4032 hydrophone, Siemens signal acquisition system, and a 360° turntable. The sensitivity of the hydrophone is -170 dB 1V/μPa. The operating frequency range of the hydrophone is from 5Hz to 120kHz and its linear frequency range is from 15Hz to 40kHz ±2dB. The sampling frequency used during the experiment was 100 kHz.

The hydrophone was submerged using a Kevlar rope to measure and receive the radiated noise signals, while also recording the underwater depth and distance from the UUV model. The Siemens signal acquisition system, located within the experimental station, was responsible for receiving and collecting signals from the hydrophone. The collected data were then processed and analyzed using a laptop computer. The UUV model was mounted on a fixed-length boom and positioned underwater, where it was rotated at a uniform speed by the 360° turntable.

TESTING ARRANGEMENT

The experiment on the lake was conducted in the open waters of Thousand Island Lake, with the experimental setup as illustrated in Fig. 2. Due to the high cost of our experimental equipment and the complex environment during field tests, including deep water depths, there is a risk of losing control and losing the UUV if it operates unrestrained in the water. Therefore, during experiment, we secure the UUV on a turntable for operation. The UUV was placed 10 m below the water surface, with the receiving array located 2 m from the model's center, both suspended horizontally. The UUV center and the hydrophone were aligned at the same depth. The test object was connected to the turntable via a flange plate, allowing for 360° rotation to measure the radiated sound pressure from different directions.

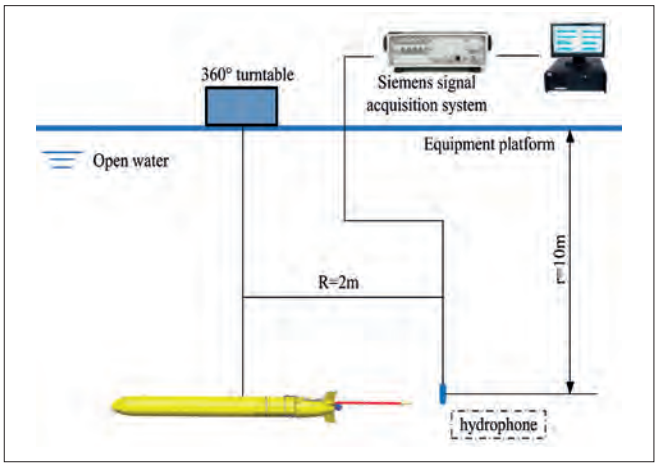

Fig. 2. Schematic diagram of the radiated sound test system

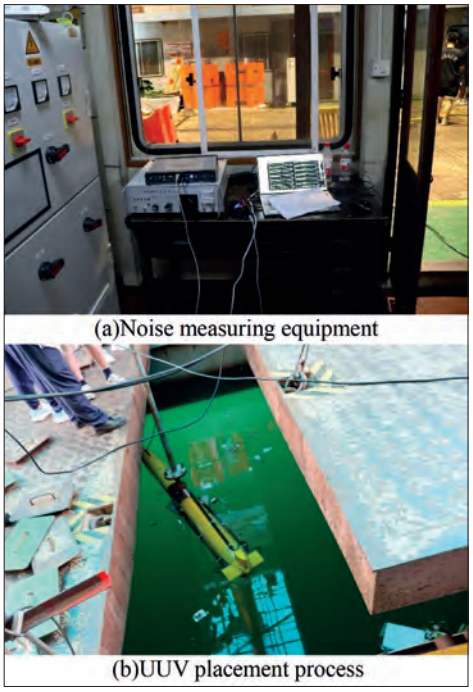

Fig. 3. Test layout site

SIMULATION MODELING

PROPELLER MODELING

The UUV's propeller used in the experiment is the Model 260 propeller produced by Tecnadyne, as shown in Fig. 4. According to the data provided on the official website, a three-dimensional model including propeller blades, hub, and the annular duct is developed using the SolidWorks software as shown in Fig. 5. The main parameters are listed in Table 1.

Fig. 4. Model 260 propeller

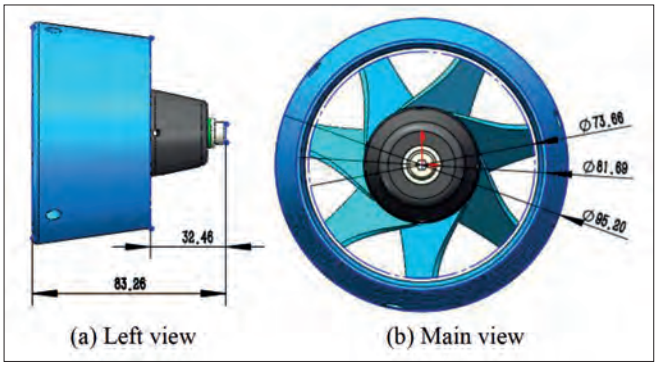

Fig. 5. Three-dimensional model of ducted propeller

Tab. 1. Main parameters of Model 260 propeller

Parameter	Value
Number of blades	7
Number of duct support columns	3
Diameter of impeller D/mm	73.66
Inlet diameter /mm	95.20
Outlet diameter /mm	81.69
Duct length /mm	50.80
Wheel hub ratio	0.45

COMPUTING DOMAIN AND BOUNDARY CONDITIONS

Propeller noise is a significant source of underwater acoustic radiation noise from UUV, with the noise measured at the stern of the UUV primarily originating from the propeller. To maintain consistency with the experimental boundary conditions and avoid differences in hydrodynamic loads between simulation and experiment, the effect of the UUV hull on the acoustic radiation at the stern is considered. Generally, there are two methods for the numerical simulation of propellers, which are the Sliding Mesh (SM) method and the Moving Reference Frame (MRF) method. This simulation utilized the Sliding Mesh method, which more closely aligns with the actual operation of the propeller by dividing the flow field into stationary and rotating regions. The main dimensions are shown in Fig. 6.

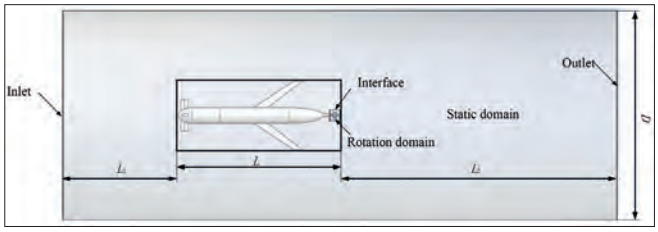

Fig. 6. Main size distribution of flow field

The UUV model has an overall length of L = 2.035 m and a maximum hull diameter of D_{max} = 0.221 m. To avoid interference from the propeller's rotation on the surrounding flow field and the impact of the choice of turbulence model on computational efficiency and accuracy, the UUV model is placed in the center of a cylindrical flow field. The diameter of the cylinder is $D > 10D_{max}$= 3 m, the length upstream of the vessel is L_1 = 1.564 m, approximately equal to one vessel length; the length downstream of the flow field is L_1 = 4 m, greater than two vessel lengths. The upstream of the flow field is the inlet, and the downstream is the outlet.

In unstructured grid systems, the commercial tool ANSYS Fluent Meshing was used to generate tetrahedral meshes, as shown in Fig. 7. The total number of mesh elements is 1736953. Mesh refinement was applied to the propeller and interface areas with grid sizes of 1 mm and 10 mm, respectively. The computation, utilizing 40 cores, is expected to take approximately 20 hours.

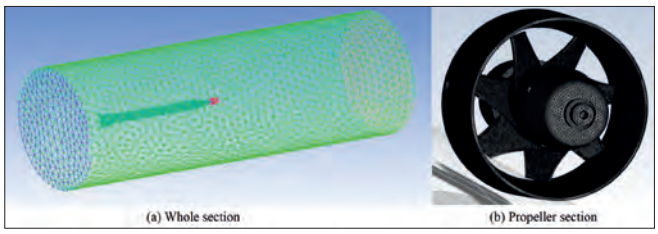

Fig. 7. Meshes of flow field and propeller section

Since cavitation is not involved in this study, the fluid in the flow field is set to default liquid water. As the model is fixed to a boom and does not move forward in the water, the simulation settings are adjusted to match the experimental state by using a pressure inlet and pressure outlet, both with a pressure value of 0. The interface between the rotating and stationary domains is defined to facilitate the exchange of flow field data between the dynamic and static areas. The FW-H equation is activated to designate the noise source as the propeller, with settings for the sound source, speed of sound, and reference sound pressure

established. The rotational speed of the rotating domain is set to the experimental values of 711.6 RPM, 898.8 RPM, 1164 RPM, and 1282.8 RPM.

Finally, the settings for the solution method are established. The solver uses the SIMPLE algorithm, and the discretization method is chosen as the second-order upwind scheme. The time step is defined as 1×10^{-4} seconds, with a total of 50000 steps, amounting to a total time of 5 seconds, satisfying the Courant number condition: $C_0 = v\frac{\nabla t}{L_0} < 100$, where is the main flow velocity, L_0 is the minimum size of the mesh elements, and ∇t is the transient time step.

RESULTS ANALYSIS

NOISE MEASUREMENT TEST RESULTS

During the experiment, the hydrophone was positioned directly opposite the stern of the UUV. After starting the UUV and allowing it to stabilize, measurements of sound pressure of the propeller's radiated noise at the stern were taken. The formula for calculating sound pressure level is: $SLP = 20\log_{10}\frac{P_e}{P_{ref}}$, where P_e is effective value of sound pressure, P_{ref} is reference sound pressure. The reference sound pressure in water is $1e^{-6}$ Pa. Fig. 8 presents the measurement results of the propeller noise at different rotational speeds. To further observe the spectral characteristics, sound pressure level of the propeller noise in frequency range from 10Hz-1000Hz are depicted in Fig. 9, which can clearly illustrate the shaft frequency and harmonic characteristics corresponding to different speeds.

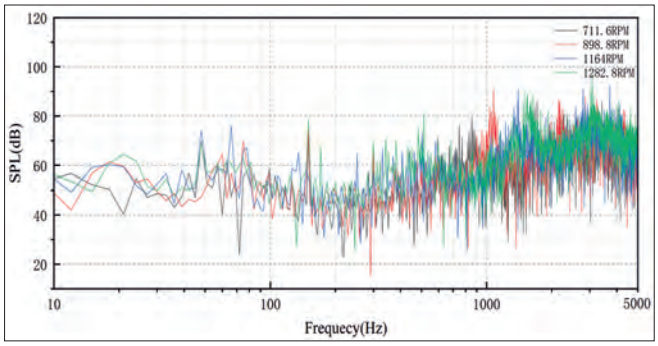

Fig.8. Sound pressure level comparison of propeller noise at different rotational speeds in frequency domain from 10 Hz up to 5 kHz

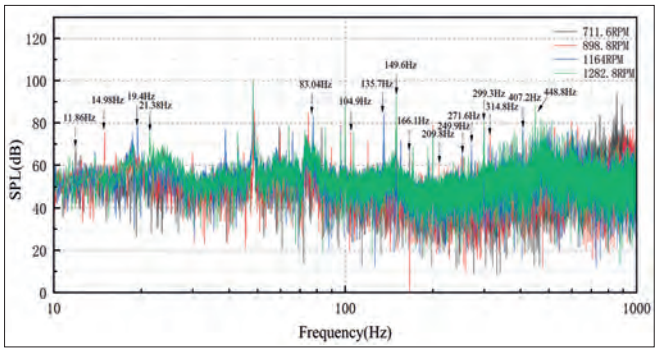

Fig.9. Sound pressure level comparison of propeller noise at different rotational speeds in frequency domain from 10 Hz up to 1 kHz

In the experiment, the rotational speeds of the propeller were fixed at 1000 RPM, 1200 RPM, 1500 RPM, and 1600 RPM. It can be observed in Fig. 9, the fundamental frequencies corresponding to these rotational speeds are 11.86 Hz, 14.98 Hz, 19.4 Hz, and 21.38 Hz, respectively. But according to the rotational speeds set by the controller, the fundamental frequencies should have been 16.67 Hz, 20 Hz, 25 Hz, and 26.67 Hz, which are calculated based on the formula $f = \frac{N}{60}$, where N is revolutions per minute. The formula for calculating blade frequency is $F = f \cdot n$, where n is number of blades. The discrepancies between the observed and theoretical frequencies can be attributed to instability in the propeller's underwater rotational speed, where the actual speed differs significantly from the set speed controlled by the controller, resulting in varying fundamental frequencies. Due to the lack of a speed feedback system, it is not possible to determine the actual propeller speed. Through analysis of the fundamental frequency, blade frequency, and harmonics at different speeds, the actual rotational speeds of the UUV underwater were determined to be 711.6 RPM, 898.8 RPM, 1164 RPM, and 1282.8 RPM. For convenience of comparison with subsequent simulations, the actual propeller speeds were used. A distinct peak around 48.27 Hz, observed across different speeds, is speculated to be caused by electrical signals. It is also noted from the figures that the sound pressure level increases with propeller speed increase, especially for the shaft frequency and the blade-passing frequency.

Tab. 2. Comparison of total test sound levels at different rotational speeds

Rotate speed /RPM	The overall sound pressure level of the experiment /dB
711.6	118.72
898.8	121.80
1164.0	124.36
1282.8	126.78

The experimental data indicates that the overall sound pressure level of propeller noise increases with the propeller's rotational speed as shown in Table 2. With the increase of the propeller speed, the overall sound pressure level of propeller noise also increases. The highest sound level is 126.78 dB at the maximum speed, and the lowest is 118.72 dB at the minimum speed. The difference in sound levels related to various rotational speeds can be also observed, with a 2.42 dB increase for a 118.8 RPM speed difference and a 2.56 dB increase for a 265.2 RPM difference.

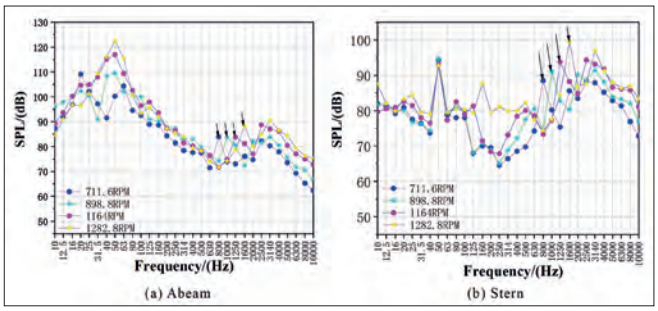

Fig. 10. 1/3 octave diagram of propeller noise at different speeds

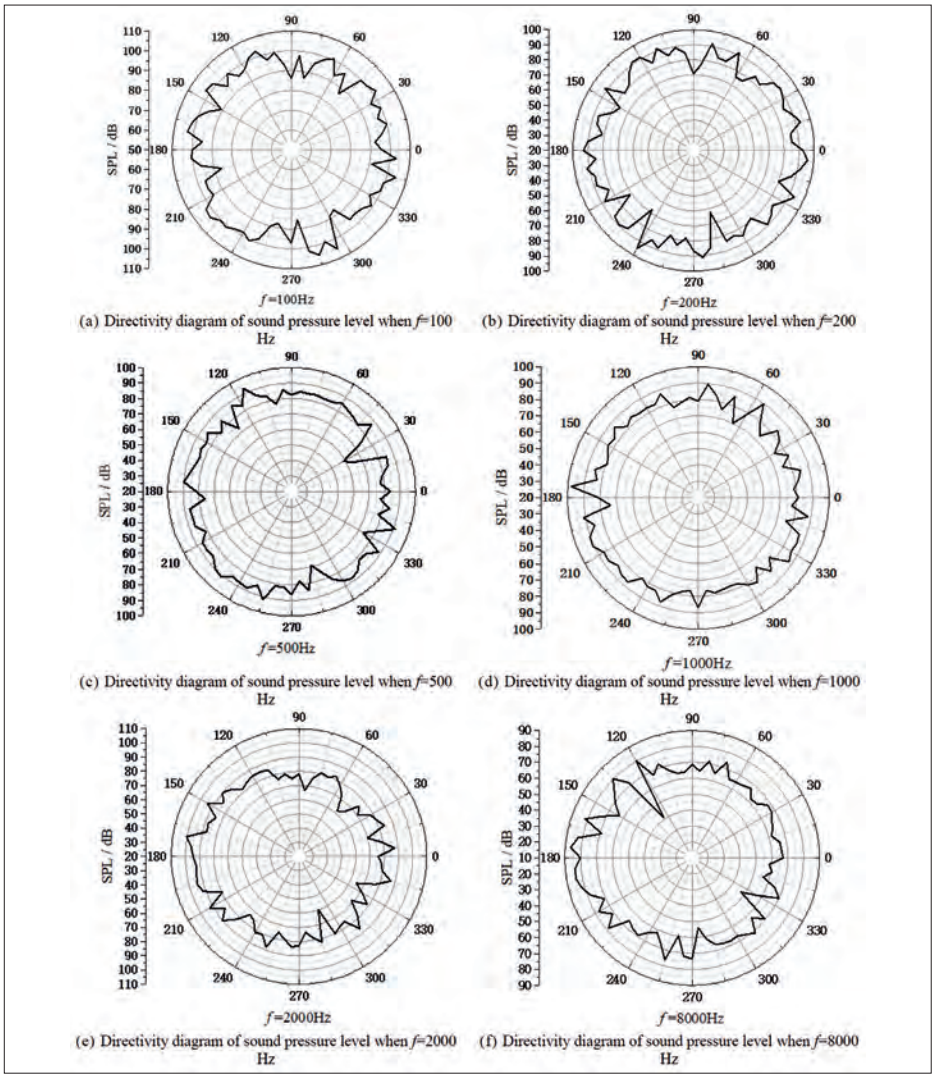

Fig. 11. Directivity of radiated noise when UUV runs at 711.6 RPM

The observation from Fig. 10 highlights that within the low-frequency range for 0-50 Hz, the level of radiated noise increases with the propeller's rotational speed. There is a significant peak at 50 Hz, primarily attributed to the influence of electrical signals. Between 100 Hz and 500 Hz, the sound pressure levels produced by different propeller speeds do not vary significantly and tend to decrease with frequency increasing. The amplitude of the sound pressure level increase obviously after 500 Hz. Distinct peaks can be found between frequency range from 800 Hz to 1600 Hz, which are corresponded to the propeller speeds. The higher the rotational speed, the higher the amplitude of the sound pressure level at the peaks. It is also noted that beyond 2000 Hz, the radiated noise for different speeds begins to attenuate, with a roughly equal rate of decay.

During the experiment, the UUV was fixed on an electric turntable, and the hydrophone was positioned 2 meters away from the UUV's center, ensuring that the UUV rotated at a constant speed. The collected data were segmented into 72 parts, each corresponding to a specific point, and connecting these 72 points provided a directivity pattern. Fig. 11 shows the directivity patterns at frequencies of 100 Hz, 200 Hz, 500 Hz, 1000 Hz, 2000 Hz, and 8000 Hz for a rotational speed of 711.6 RPM. The patterns generally exhibit symmetric characteristics, with 0° aligning with the UUV's bow and 180° with the stern, where the noise is slightly higher than at the bow, although the patterns are not perfectly symmetrical. This asymmetry mainly results from the manual adjustment of the UUV's horizontal position during the experiment, leading to uneven rotation. Furthermore, the exact underwater posture of the UUV is unclear, as sometimes it does not return precisely to its original position after completing a rotation, causing the 0° point not to align perfectly with the bow. Before submerging the UUV underwater for testing, the bow corresponding to 0° is marked to determine the orientation of the UUV during operation underwater. The UUV is marked and its position recognized underwater through rigid linkage connections. The UUV is connected to a rigid linkage via a flange, with the top of the linkage connected to an electric turntable. The electric turntable rotates uniformly at a speed of 3 degrees per second under the control of a controller. This setup ensures that the UUV rotates steadily underwater. Despite these issues, the directivity pattern clearly shows that the radiated noise is relatively higher at the bow and stern.

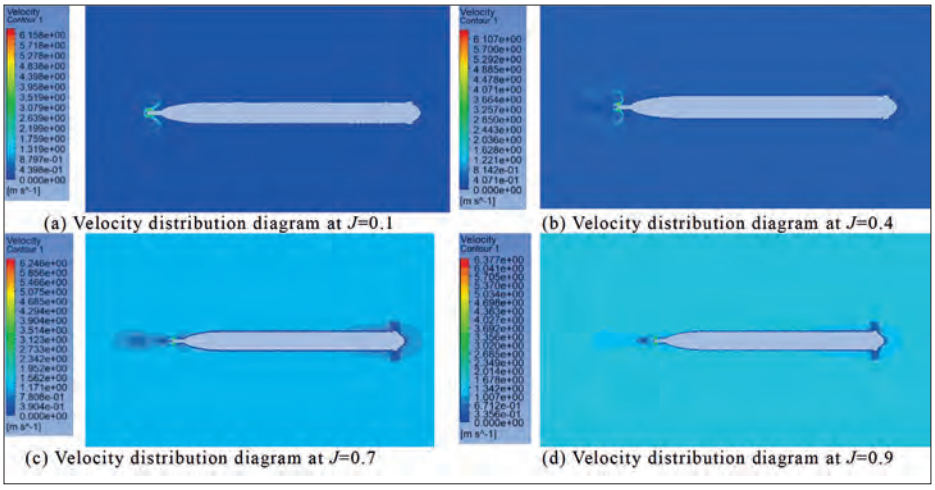

Fig.12. Velocity distribution diagram in axial section of downflow field with different advance velocity coefficients

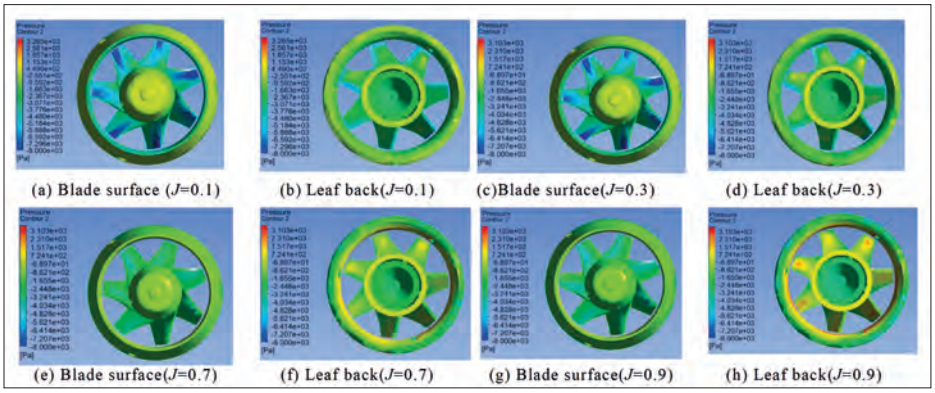

Fig.13. Pressure distribution diagram on propeller surface

FLOW FIELD CALCULATION RESULTS AND ANALYSIS

Utilizing Fluent software for steady-state flow field simulation, the setup involves fixing the rotational speed at 1282.8 RPM and varying the inlet velocities to simulate flow fields under different advance coefficients. The axial velocity distribution in the flow field for varying advance coefficients is illustrated in Fig. 12.

From Fig. 12, it is observed that a pair of vortices with opposite rotational directions form on either side of the propeller's wake, and these vortices cover a larger area when the advance coefficient is lower. As the fluid diffuses and develops downstream, the impact of the propeller blades becomes increasingly significant. Eventually, the areas with higher flow velocity bifurcate into two streams that diffuse outward. With the increase in the advance coefficient, the stratification of the flow lines becomes more pronounced, and concurrently, the efficiency of the propeller improves.

The pressure distribution on the propeller surface under different advance coefficients, as shown in Fig. 13, reveals that as the advance coefficient J increases, the pressure on the propeller blade surfaces gradually decreases. However, the overall distribution of pressure does not undergo significant change, the pressure on the suction side which back of the blade remains higher than on the pressure side which face of the blade. The maximum and minimum pressures occur along the leading edge, and the differential pressure between the blade's suction and pressure sides generates thrust.

When the propeller speed is fixed at 1282.8 RPM and the position of the monitoring point remains unchanged, the propeller noise sound pressure level under different advance coefficients J is compared, as shown in Fig. 14. Because the propeller speed mentioned in this paper has not caused cavitation phenomenon after calculation and analysis, the simulation calculation of cavitation phenomenon is not involved in this paper.

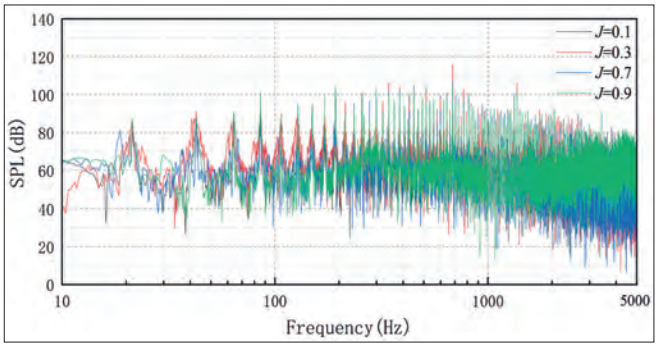

Fig. 14. Comparison of sound pressure levels under different advance coefficients J

As can be seen from Fig. 13, the sound pressure level of the propeller also increases with the increase of the advance coefficient J. This is because at high flow rates, the rotation of the

propeller causes the surrounding area to have higher turbulent pulsations, resulting in greater pressure fluctuations.

SOUND FIELD CALCULATION RESULTS AND ANALYSIS

Using Fluent software, the flow field around the propeller was simulated, and then the FW-H equation was employed to predict propeller noise. The comparison between simulation calculations and experimental test results is presented in Fig. 15.

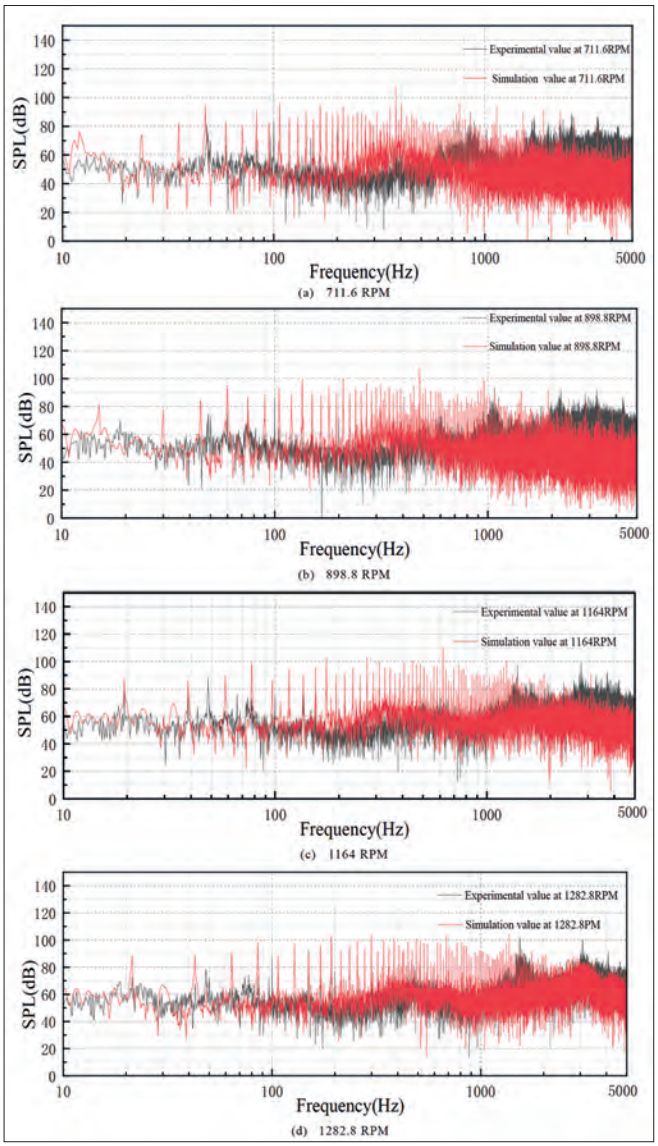

Fig. 15. Comparison of simulation and test values of propeller noise at different rotational speeds

The comparison between the simulated and experimental values of the propeller noise sound pressure level across different rotational speeds reveals a generally consistent trend within the 0-5000 Hz frequency range. Notably, the simulation values are relatively higher than the experimental values between 100 Hz and 1000 Hz, with this discrepancy being particularly evident between 100 Hz and 400 Hz. This frequency range prominently features line spectrum peaks corresponding to shaft and blade frequencies, and the peak frequencies in the line spectra from both the experimental and simulation results are essentially aligned. For frequencies between 1000 Hz and 5000 Hz, the experimental values are higher than those from the simulations. The experimental and simulation values match more closely at higher rotational speeds compared to lower speed, mainly focusing on shaft frequency, blade frequency, and multiple shaft frequencies. The line spectrum characteristics are more pronounced in the simulation results than in the experimental outcomes, largely because the simulation model is more idealized, rendering the shaft frequencies clearer.

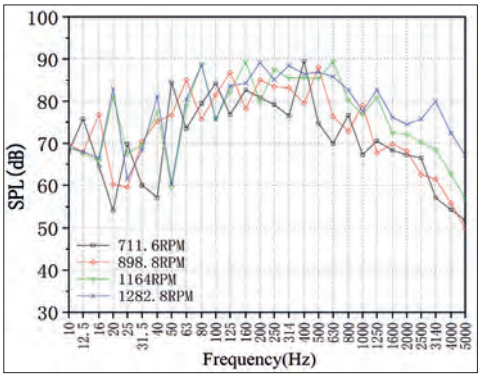

Fig. 16. 1/3 octave diagram of propeller noise at different speeds

As illustrated in Fig. 16, the third-octave band chart of propeller noise simulated at different rotational speeds shows that, within the low-frequency range of up to 50 Hz, the radiated noise values generally increase with rising rotational speeds. Between 100 Hz and 500 Hz, the sound pressure levels generated by different propeller speeds do not vary significantly. However, beyond 500 Hz, the amplitude begins to increase with frequency, and clear peaks are observed between 800 Hz and 1600 Hz, each corresponding to the propeller's rotational speed the higher the speed, the higher the frequency of the peak. Additionally, it's noted that after 2000 Hz, there's a trend of decreasing radiated noise.

CONCLUSIONS

This article initially conducts underwater radiated noise experiments for UUVs at lake's hydroacoustic test field, followed by a computational analysis of UUV hydrodynamics and radiated noise based on numerical methods. By comparing the simulation results with the experimental test results, the accuracy of both simulations and experiments is verified. Further, based on the results of experiments and numerical calculations, a detailed analysis of the noise characteristics of UUV underwater radiated noise is conducted. The main conclusions of the article are as follows:

(1) The experimental results show that within the low-frequency range, the amplitude differences in the radiated sound pressure levels produced by the propeller are miniature. Between 25 Hz and 80 Hz, there is a significant difference in the noise spectrum in the lateral direction, and in the stern direction, the noise spectrum mainly shows

significant differences between 100 Hz and 500 Hz, with higher rotational speeds resulting in higher sound pressure levels. Between 800 Hz and 1600 Hz, there are clear peak values, which match the propeller's rotational speed. Beyond 3000 Hz, there is a noticeable downward trend in the sound pressure level.

(2) The overall trend of the simulated and experimental values of propeller noise at different rotational speeds is consistent, with the simulated sound pressure levels being slightly higher than the experimental test values. In the numerical results, the line spectrum characteristics are more pronounced within the 100 Hz to 400 Hz range, mainly because the simulation model is more idealized compared to the experimental tests.

REFERENCES

1. Xiaohong Li, Shuanghe Yu, Xiaozhi Gao, Yan Y, Ying Z. Path planning and obstacle avoidance control of UUV based on an enhanced A* algorithm and MPC in dynamic environment. Ocean Eng. 2024, 302: 117584. https://doi.org/10.1016/j.oceaneng.2024.117584.

2. Zheping Yan, Jinyu Yan, Fangbo Nan, Sijia Cai, Shuping Hou. Distributed TMPC formation trajectory tracking of multi-UUV with time-varying communication delay. Ocean Eng. 2024, 117091. https://doi.org/10.1016/j.oceaneng.2024.117091.

3. Xiaowei Yan, Hao Song, Zilong Peng, Huimin Kong. Review of research results concerning the modelling of shipping noise. Pol Marit Res. 2021, 28(2):102-115. https://doi.org/10.2478/pomr-2021-0027.

4. Drężek M, Augustyniak M. Universal sea/fem based method for estimation of vibroacoustic coupling loss factors in realistic ship structures. Pol Marit Res. 2024, 31: 55-63. https://doi.org/10.2478/pomr-2024-0006.

5. Kozaczka E, Grelowska G. Propagation of ship-generated noise in shallow sea. Pol Marit Res. 2018, 25(2):37-46. https://doi.org/10.2478/pomr-2018-0052.

6. Qiaorui Si, Asad Ali, Ding Tian, Mengfei Chen, Xiao BC, Jian JY. Prediction of hydrodynamic noise in ducted propeller using flow field-acoustic field coupled simulation technique based on novel vortex sound theory. Ocean Eng. 2023, 272: 113907. https://doi.org/10.1016/j.oceaneng.2023.113907.

7. Xuehao Wang, Yanhui Wang, Peng Wang, Shaoqiong Yang, Wendong Niu, Yehao Yang. Design, analysis, and testing of Petrel acoustic autonomous underwater vehicle for marine monitoring. Phys. Fluids. 2022, 34:037115. https://doi.org/10.1063/5.0083951.

8. Lei Liu, Zengwu Zhao, Juan Wei, Xiaobei Li, Liwei Yuan. Simulation of shock test for an AUV propulsion motor based on DDAM. Journal of Physics: Conference Series. IOP Publishing. 2021, 2029:012037. https://doi.org/10.1088/1742-6596/2029/1/012037.

9. Kowalczyk S, Felicjancik J. Numerical and experimental propeller noise investigations. Ocean Eng. .2016, 120108-115. https://doi.org/10.1016/j.oceaneng.2016.01.032.

10. Bhattacharyya A, Krasilnikov V, Steen S. A CFD-based scaling approach for ducted propellers. Ocean Eng. 2016, 123: 116-130. https://doi.org/10.1016/j.oceaneng.2016.06.011.

11. Denghui Qin, Guang Pan , Lee S, Qiaogao Huang, Yao Shi. Underwater radiated noise reduction technology using sawtooth duct for pumpjet propulsor. Ocean.Eng. 2019, 188(July), 106228.1-106228.15 https://doi.org/10.1016/j.oceaneng.2019.106228.

12. Mengfei Chen, Jinfeng Liu, Qiaorui Si., Liang Yun, Zhongkun Jin, Jianping Yuan. Investigation into the hydrodynamic noise characteristics of electric ducted propeller, J. Mar. Sci. Eng. 2022, 10 (3). https://doi.org/10.3390/jmse10030378.

13. Kimmerl J, Mertes P, Abdel-Maksoud M. Application of large eddy simulation to predict underwater noise of marine propulsors. Part 2: Noise generation. J. Mar. Sci. Eng. 2021, 9: 778. https://doi.org/10.3390/jmse9080792.

14. Chamanara M, Ghassemi H. Hydrodynamic characteristics of the kort-nozzle propeller by different turbulence models. Am. J. Mech. Eng. 2016. 4:169-172. https://doi.org/10.12691/ajme-4-5-1.

15. Wencan Zhang, Lihong Wu, Xiangwei Jiang, Xisheng Feng, Yiping Li, Junbao Zeng, Chongde Liu. Propeller Design for an Autonomous Underwater Vehicle by the Lifting-line Method based on OpenProp and CFD. J Mar Sci Appl. 2022, 21(2): 106-114. https://doi.org/10.1007/s11804-022-00275-w.

16. Lee T, Ahn BK, Lee K, Lee Y, Kim HJ. Prediction of cavity inception speed and underwater radiated noise of a full-scale marine propeller based on a cavitation tunnel model test. Ocean Eng. 2024, 118456. https://doi.org/10.1016/j.oceaneng.2024.118456.

17. Viitanen V, Sipilä T, Sánchez-Caja T, Siikonen T. CFD predictions of unsteady cavitation for a marine propeller in oblique inflow. Ocean Eng. 2022.112596. https://doi.org/10.1016/j.oceaneng.2022.112596.

18. Ku G, Cho J, Cheong C, Seol H. Numerical investigation of tip-vortex cavitation noise of submarine propellers using hybrid computational hydro-acoustic approach. Ocean Eng. 2021, 109693. https://doi.org/10.1016/j.oceaneng.2021.109693.

19. Railey K, Dibiaso D, Schmidt H. An acoustic remote sensing method for high-precision propeller rotation and speed

estimation of unmanned underwater vehicles. J. Acoust. Soc. Am. 2020, 148(6): 3942-50. https://doi.org/10.1121/1.4754419.

20. Gebbie J, Siderius M, Allen JS. Aspect-dependent radiated noise analysis of an underway autonomous underwater vehicle. J. Acoust. Soc. Am. 2012, 132(5). https://doi.org/10.1121/1.4754419.

21. Changli Yu, Renzhi Wang, Xingming Zhang, Yueming Li. Experimental and numerical study on underwater radiated noise of AUV. Ocean Eng. Volume 201, 1 April 2020, 107111. https://doi.org/10.1016/j.oceaneng.2020.107111.

22. Zakeri E, Farahat S, Moezi SA, Zare A. Robust sliding mode control of a mini unmanned underwater vehicle equipped with a new arrangement of water jet propulsions: Simulation and experimental study. Appl. Ocean Res. Volume 59, September 2016, Pages 521-542. https://doi.org/10.1016/j.apor.2016.07.006.

23. Zhiwei Si, Shuaikang Shi, Xiuchang Huang, Zhiqiang Rao, Hongxing Hua. Vibro-acoustic characteristics of a coupled pump-jet hafting system-SUBOFF model under distributed unsteady hydrodynamics by a pump-jet. Ocean Eng. Volume 235, 1 September 2021, 109429. https://doi.org/10.1016/j.oceaneng.2021.109429.

24. Xuehao Wang, Yanhui Wang, Peng Wang, Shaoqiong Yang, Wendong Niu, Yehao Yang. Design, analysis, and testing of Petrel acoustic autonomous underwater vehicle for marine monitoring. Phys. Fluids. 2022, 34. https://doi.org/10.1063/5.0083951.

25. Qindong Sun, Hongkun Zhou. An Acoustic Sea Glider for Deep-Sea Noise Profiling Using an Acoustic Vector Sensor. Pol Marit Res. 29(1):57-62. https://doi.org/10.2478/pomr-2022-0006.

26. Buszman, K. Analysing the Impact on Underwater Noise of Changes to the Parameters of a Ship's Machinery. Pol Marit Res. https://doi.org/10.2478/pomr-2020-0059. September 202027(3):176-181.